

A rebinding-assay for measuring extreme kinetics using label-free biosensors

John G Quinn (✉ quinnj6@gene.com)

Biophysical Group, Biochemical and Cellular Pharmacology, Genentech Inc., 1 DNA Way, South San Francisco, CA 94080

Research Article

Keywords: In Vitro Kinetic Measurements, Mechanistic Characterization, Binding Interactions, Drug Discovery, Transient Kinetics, Probe-based Assay

Posted Date: March 6th, 2021

DOI: <https://doi.org/10.21203/rs.3.rs-273255/v1>

License:  This work is licensed under a Creative Commons Attribution 4.0 International License.

[Read Full License](#)

Version of Record: A version of this preprint was published at Scientific Reports on April 15th, 2021. See the published version at <https://doi.org/10.1038/s41598-021-87880-x>.

Title Page

A rebinding-assay for measuring extreme kinetics using label-free biosensors

Author and corresponding author: John G. Quinn (email: quinnj6@gene.com)

Correspondence and requests for materials should be addressed to John G. Quinn (email: quinnj6@gene.com)

Authors is a member of the following organization: Biophysical group, Biochemical and Cellular Pharmacology, Genentech Inc., 1 DNA Way, South San Francisco, CA 94080

A rebinding-assay for measuring extreme kinetics using label-free biosensors

John G. Quinn

Biophysical group, Biochemical and Cellular Pharmacology, Genentech Inc., 1 DNA Way, South San Francisco, CA 94080

Correspondence and requests for materials should be addressed to John G. Quinn (email: quinnj6@gene.com)

Abstract

In vitro kinetic measurements allow mechanistic characterization of binding interactions and are particularly valuable throughout drug discovery, from confirmation of on-target binding in early discovery to fine-tuning of drug-binding properties in pre-clinical development. Early chemical matter often exhibits transient kinetics, which remain challenging to measure in a routine drug discovery setting. For example, characterization of irreversible inhibitors has classically relied on the alkylation rate constant, yet this metric fails to resolve its fundamental constituent rate constants, which drive reversible binding kinetics and affinity complex inactivation. In other cases, extremely rapid association processes, which can approach the diffusion limit, also remain challenging to measure. To address these limitations, a practical kinetic rebinding assay is introduced that may be applied for kinetic screening and characterization of compounds. The new capabilities afforded by this probe-based assay emerge from mixed-phase partitioning in a flow-injection configuration and have been implemented using label-free biosensing. A finite element analysis-based biosensor model, simulating inhibition of rebinding within a crowded hydrogel milieu, provided surrogate test data that enabled development and validation of an algebraic model for estimation of kinetic interaction constants. An experimental proof-of-principle demonstrating estimation of the association rate constant, decoupled from the dissociation process, provided further validation.

Introduction

In vitro kinetic assays are valuable throughout drug discovery, particularly during hits-to-leads progression, by providing mechanistic discrimination of artifactual binding^{1, 2, 3} from tractable binding modes. Routine kinetic measurements also allow compounds to be optimized towards a desirable target-specific kinetic profile^{4, 5, 6} allowing fine tuning of compound properties, including target engagement and residence time for enhanced clinical efficacy⁷. Indeed, routine measurement of direct binding kinetics using real-time label-free biosensors^{8, 9} provides a practical means of leveraging kinetics for compound prioritization yet the transient kinetics of early chemical matter largely remains beyond the limit of detection. To date, transient kinetics, defined here as affinity complexes that fully dissociate in $< 1s$, are measured using low throughput stop-flow based methods¹⁰, which are impractical for analysis of compound collections in a drug discovery setting. A biosensor-based approach has recently been reported¹¹, addressing this limitation but specific system customizations are required to enable routine application. Probe-based kinetic competition assays¹² are readily adapted to achieve the necessary throughput and may be implemented using surface plasmon resonance (SPR)-based biosensor technology¹³, or equivalent flow-injection-based platform, but regrettably are also insensitive to transient kinetics. Here, we introduce a probe-based kinetic rebinding assay that allows association rate constants to be measured up to the diffusion limit, which are challenging to measure by direct label-free binding kinetics¹⁴. This probe-based assay is insensitive to both bulk-refractive index mismatches and baseline drift signal and is particularly valuable for estimating transient kinetics associated with mechanistically complex inhibitors, such as irreversible inhibitors. Biophysically realistic in-silico biosensors^{11, 14, 15} based on finite element computational modeling have provided realistic surrogate data for validation of mechanistic binding models in the past and this approach was adopted for development and validation of the rebinding assay.

Results

Principle of rebinding-assay. The sensing region of the biosensor system and associated reaction/diffusion pathways for the rebinding assay are illustrated in Fig. 1 and were modelled using a finite element analysis-based computational model in order to produce surrogate experimental data to develop, and validate, an algebraic model suitable for estimation of kinetic constants from inhibition of rebinding curves. Coupled partial differential equations were discretized over space (the physical geometry) and time and solved by finite element analysis (see Supplemental Note Virtual Instrument).

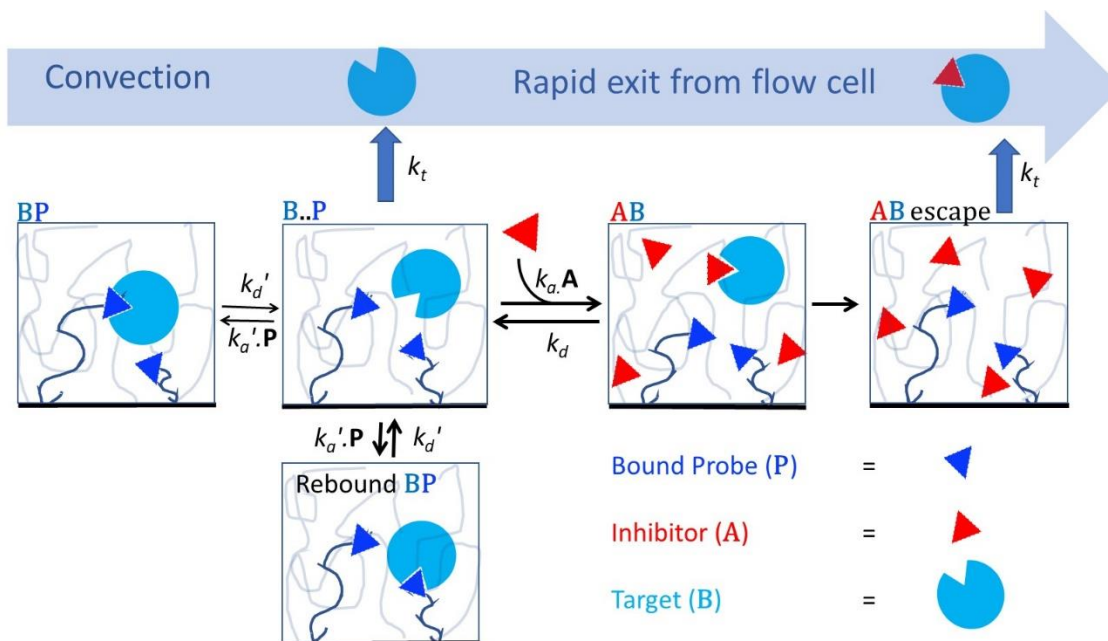


Fig. 1. Reaction/diffusion pathways of biosensor-based rebinding-assay. A hydrogel, depicted here as random loops, is derivatized to possess a high concentration of P (blue triangle), which is competitive with inhibitor A (red triangle) in binding to target B (blue circle). Paired forward- and reverse-rate constants for formation of BP and AB are $k_a' (M^{-1}s^{-1})/k_d' (s^{-1})$ and $k_a (M^{-1}s^{-1})/k_d (s^{-1})$, respectively, while $k_t (s^{-1})$ is the mass transport coefficient that defines the hydrogel escape rate. The molecular contacts stabilizing BP dissociate releasing B to become a transient species B.P that can readily reform BP, pairing with any P in its vicinity. Multiple rebinding cycles are favored at higher concentrations of B and high k_a' before B escapes the sensing region at rate k_t . Injected A sequesters B thereby depleting B.P forming AB, which in turn exits the hydrogel thereby negating rebinding. However, in the case that AB dissociates before exiting, then liberated B will revert to B.P. Although not depicted here, B that has escaped the hydrogel has a probability of re-entering the hydrogel further downstream again replenishing B.P. See Supplemental Note Fig. 1 for more details.

The flux balance in B for surface reaction relative to mass transport from bulk liquid determines the degree of mass transport limitation, which slows binding and promotes rebinding, and may be expressed by the dimensionless Damköhler number (Da), expressed here in terms of biosensor response as;

$$Da = k_a' (R_{\max} - R) / k_t \quad (1)$$

where $R_{\max} - R \propto P$, R_{\max} is the biosensor response at surface saturation, R is the response at any given time and $k_t (s^{-1})$ is the mass transport coefficient¹⁶. k_t defines the rate at which B may enter, or escape, the mass transport boundary layer that forms over the sensing region. The escape time $\tau = 1/k_t$ is typically in the ms-regime and

confers extraordinary sensitivity to transient kinetics. An expression for k_t that accounts for mass transport resistance through the flow cell and through the hydrogel may be defined by the approximation;

$$k_t = T_\gamma 1.281 \cdot \left(\frac{v_c \cdot D}{2 \cdot h \cdot l} \right)^{1/3} \quad (2)$$

where v_c = maximum flow velocity at center of flow channel (m/s), D = diffusion coefficient of analyte in bulk liquid (m^2/s), h = flow cell height (m) and l = length of functionalized sensing region (m) upstream, and including, the optically interrogated region. The incorporation of a hydrogel transport resistance term T_γ is required to account for hydrogel transport resistance¹⁷. This term is defined by the height of the hydrogel H_{gel} relative to the mean free path taken by **B** before being bound where $T_\gamma = \text{Tanh}(\gamma)/\gamma$, with $\gamma = H_{\text{gel}} / (D_{\text{gel}} \cdot K_{\text{part}} / (k_a \cdot \mathbf{P}))^{0.5}$, where K_{part} = hydrogel partition coefficient (unit less) and D_{gel} = diffusion coefficient of **B** within the hydrogel (m^2/s). A mass transport coefficient may be expressed in terms of biosensor response as $k_t' = 10^9 \cdot M_{r,B} \cdot k_t$, where 10^9 is a response unit scaling factor (g m/mol) and $M_{r,B}$ = molecular weight of **B** (g/mol).

Equations (1) and (2) can be used to guide experimental design and imply that rebinding increases with increasing k_a' , increasing \mathbf{P} , increasing hydrogel thickness and decreasing flow rate. Equation (2) allows approximation of k_t where hydrogel parameters (e.g. H_{gel} , D_{gel} , K_{part}) are available but it is generally estimated as a fitted parameter when fitting kinetic models to direct binding progress curves¹⁴. The simulated binding curves in Fig. 2 show that mass transport resistance results in slowing of both association- and dissociation-phase curves as a function of increasing mass transport resistance i.e. increasing Da . However, injection of an excess of **A** during the dissociation phase inhibits rebinding of **B**, restoring the true dissociation rate of **AB**, while partial inhibition occurs at lower concentrations of **A**.

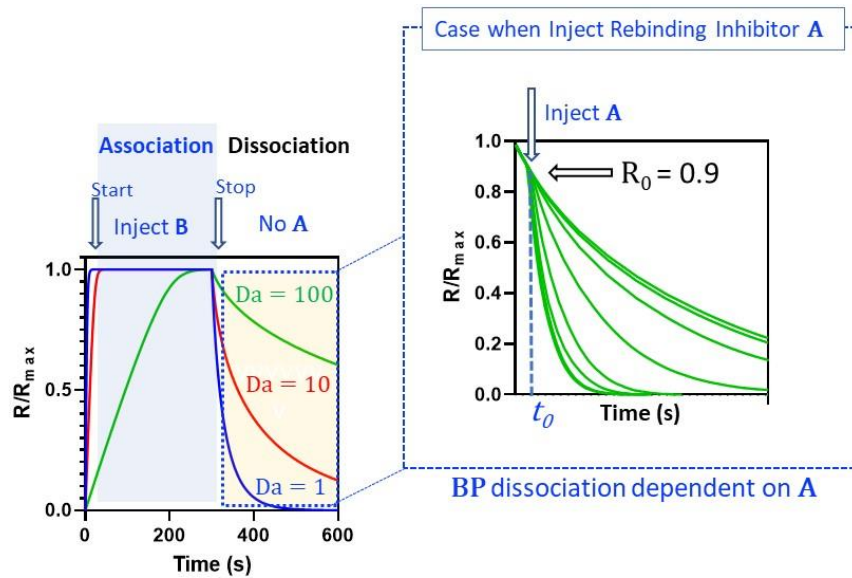


Fig. 2: Simulated binding response curves for rebinding and inhibition of rebinding. Three mass transport limited binding curves for 10 nM **B** binding to **P** tethered within a hydrogel are shown on the left. The response curves were normalized to the maximum saturation response R_{max} observed before the dissociation phase. The three simulated curves correspond to k_t values of $1 \times 10^7 \text{ s}^{-1}$, $1 \times 10^8 \text{ s}^{-1}$ and $1 \times 10^9 \text{ s}^{-1}$, producing Da values of 100, 10, 1, respectively. The simulation was performed using a two-compartment model (see Supplemental Note Fig. 2) and the interaction parameters were $R_{\text{max}} = 20 \text{ RU}$, $k_a' = 5 \times 10^7 \text{ M}^{-1}\text{s}^{-1}$ and $k_d' = 0.05 \text{ s}^{-1}$. Inhibition of rebinding during the dissociation phase at a fixed operating condition is depicted on the right, where injection of **A** over a concentration series causes dose-dependent inhibition of rebinding. The response observed at the onset (t_0) of the inhibitor injection is R_0 . Inhibition curves were simulated using the finite element computational biosensor model and is described in detail in Supplemental Note Virtual Instrument.

Inhibition of rebinding model. An optimal balance between kinetic measuring range and sensitivity to inhibition requires relatively low levels of transport limitation ($Da < 10$) which also help to maintain approximate mono-exponential behavior, as shown in the simulated inhibition of rebinding curves in Fig. 3a. Such monotonic behavior also depends on rapid development of a quasi-steady-state with respect to the competing pathways acting upon **B.P**. Free **B** is assumed to be in an unbound transient state **B.P** within the hydrogel that is partitioned by three rate coefficients, namely re-association $k_a'\mathbf{P}$ (s^{-1}), inhibition $k_a\mathbf{A}$ (s^{-1}) and hydrogel escape k_t (s^{-1}). Therefore, inhibition curves follow an approximate exponential decay where the change in response is given as;

$$R = R_0 \cdot e^{-k_{off} \cdot t} \quad (3)$$

where k_{off} (s^{-1}) is the observed dissociation rate constant.

Injection of **A** produces an inhibition rate that increases k_{off} by lowering rebinding such that $k_{off} \approx k_d'$ when fully inhibited. Rather than attempting to estimate transport and reaction fluxes from first principles, the transition state-based model described in Fig. 1 employs a phenomenological rebinding factor α , where $k_{off} = k_d' \cdot \alpha$, and is suitable for estimation of kinetic constants by fitting an exponential decay given as;

$$R = R_0 \cdot e^{-k_d' \cdot \alpha \cdot t} \quad (4)$$

$$\text{where } \alpha = \frac{\beta}{\beta + k_a' \cdot \mathbf{P}}$$

$$\text{and } \beta = k_t + f \cdot k_a \cdot \mathbf{A}, \quad f = 1 / (1 + k_d / k_t), \quad \mathbf{P} = R_{\max} / G \cdot M_r,$$

The rebinding factor α is the degree to which dissociation is slowed due to rebinding and is given by the ratio of rebinding $k_a'\mathbf{P}$ relative to hydrogel escape β . Therefore, $\alpha = 1$ when rebinding does not exist, or when rebinding is fully inhibited, otherwise $\alpha < 1$. The partition function f accounts for loss in inhibition of rebinding due to unbinding of **AB** before escaping the hydrogel. The rate constants associated with f are high relative to k_d' allowing a quasi-steady-state to be assumed. The response-to-concentration factor $G \cdot M_r$ express R_{\max} as a molar concentration of **P**, where G is the sensitivity of the biosensor to protein (1g/l) and for many SPR-based biosensors $G = 100$ RU/g/L, assuming the protein is distributed homogeneously within the hydrogel and there are experimental methods¹⁸ to estimate this parameter for higher accuracy. In practice, the optimal k_d' is defined by the optimal monitoring time, which scales as $1 / k_d' \cdot \alpha$, in order to support reasonable throughput and favors a moderate k_d' regime where $1 > 1 / k_d' > 300$ (s). The assay tolerates wide variation in k_a' since the reaction flux ($k_a' \cdot \mathbf{P}$) may be modulated by the concentration of probe but higher values (e.g. $k_a' > 1 \times 10^5 \text{ M}^{-1}\text{s}^{-1}$) are advantageous.

Estimation of k_a for non-transient inhibitors. When analyzing non-transient binders we assume $k_d \ll k_t$ and therefore $f \approx 1$ and can be neglected. The kinetics of **BP** formation, namely k_a' and k_d' , are predetermined by conventional direct binding kinetics, at low surface density of probe, prior to characterizing inhibitors. These kinetic constants are then held constant when analyzing dose-dependent inhibition curves, allowing k_a , k_d and k_t to be readily determined by global fitting equation (4). Although not essential, a zero-inhibition curve, where $\mathbf{A} = 0$, may be included to allow k_t to be estimated in the absence of inhibition, where $\alpha = k_t / (k_t + k_a' \cdot \mathbf{P})$. Pre-estimation of k_a' and k_d' by conventional direct binding kinetics may be avoided by testing the soluble probe as an inhibitor sample while also maintaining it as the surface-bound probe. In this case, **AB** becomes a fully soluble form of **BP** and hence both k_a' and k_a govern the same interaction but in reverse orientation. The associated kinetic rate constants are related through molecular weight-dependent diffusion scaling, where $k_a' \approx k_a / (M_{r,P} / M_{r,B})^{1/3}$ and substitution into equation (4) allows k_a' , k_d' and k_t to be estimated from global fitting. These parameters are then held constant when fitting unmodified equation (4) to the remainder of the inhibitor panel for estimation of k_a . We generated surrogate experimental data over a wide range in k_a , at a fixed concentration of **A**, in order to determine the relative error and confidence intervals associated with k_a -estimation for non-transient inhibitors, where $k_d \ll k_t$, producing the data show in in Fig. 3. For each curve set the upper and lower limit curves correspond to k_{off} at zero inhibition and k_d' at full inhibition, respectively. These limits define a 2-fold wider

response widow for a 10-fold higher k_a' leading to an increase in measuring range with increasing mass transport limitation (Fig. 3b, c).

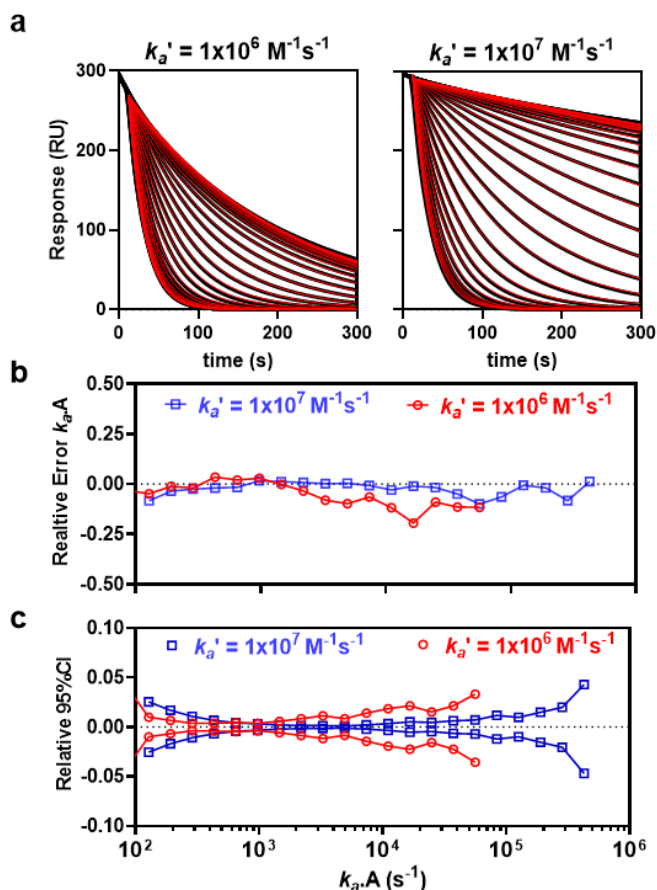


Fig. 3. Estimation of k_a from individual inhibition curves at two values of k_a' . (a) Fitted inhibition curves for moderate- (left panel $Da = 8.7$) and high- (right panel, $Da = 87$) mass transport limitation. Inhibition curves (black) were fit (red) to equation (4), where k_a was fit locally, giving independent estimates of k_a for each curve, while all other parameters were held constant. (b) Relative error in $k_a \mathbf{A}$ as a function of true $k_a \mathbf{A}$. All values where absolute relative error was < 0.2 are shown. (c) 95% confidence intervals expressed as a fraction of estimated $k_a \mathbf{A}$ and plotted versus true $k_a \mathbf{A}$ and were < 0.05 . See Supplemental Note Fig. 3 for more details.

Experimental proof-of-principle for estimating k_a of non-transient inhibitors. A soluble probe was employed as a surrogate test inhibitor in order to cross-validate parameter return since, in this particular case, we may assume $k_a \approx k_a'$ after normalization for reversal of the ligand-receptor format through diffusion scaling, where $k_a' = k_a / (M_{r,P} / M_{r,B})^{1/3}$ and the experimental data is shown in Fig. 4. Direct binding kinetics returned $k_a = 2.76 \pm 0.008 (\times 10^6) \text{ M}^{-1}\text{s}^{-1}$ for soluble-probe binding to immobilized-target (Fig. 4a) and after diffusion re-scaling this becomes $k_a = 1.0 \times 10^5 \text{ M}^{-1}\text{s}^{-1}$, which is within 15% of $k_a' = 8.5 \pm 0.004 (\times 10^4) \text{ M}^{-1}\text{s}^{-1}$ obtained for the reverse format (Fig. 4b), where soluble-target was bound to immobilized-probe. More importantly, $k_a = 2.76 \pm 0.008 (\times 10^6) \text{ M}^{-1}\text{s}^{-1}$ for direct binding of probe is within 10% of $k_a = 3.07 \pm 0.01 (\times 10^6) \text{ M}^{-1}\text{s}^{-1}$ returned from inhibition of rebinding (Fig. 4d), thereby cross-validating the results between these assay formats. The assay is compatible with a throughput of > 500 inhibitors/day using a biacore 8K (Cytiva Inc), assuming four concentrations per inhibitor. However, the assay may also be conducted in singleton for higher throughput screening facilitating analysis of medium-sized compound collections, such as fragment libraries, to be analyzed, in a single assay run.

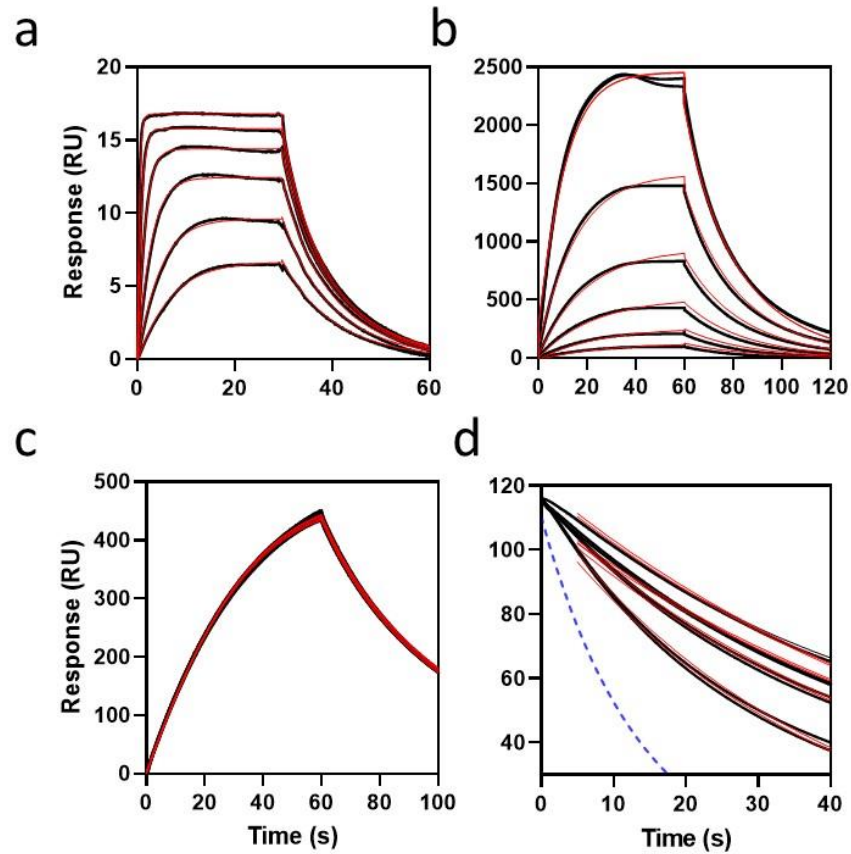


Fig. 4. Experimental estimation of k_a using the rebinding assay. (a) Conventional SPR curves (black) for interaction of soluble probe with a hydrogel-bound target ($M_r = 22$ kDa) and fit to a two-compartment 1:1 interaction model (red) for estimation of k_a and k_d . Probe ($M_r = 737$ Da) was injected for 30 s in duplicate over a serial doubling dilution range from 1 μM to 31 nM. All parameters were fit globally returning values of $k_a = 2.76 \pm 0.008$ ($\times 10^6$) $\text{M}^{-1}\text{s}^{-1}$, $k_d = 0.125 \pm 0.0003$ s^{-1} , $R_{\text{max}} = 16.8 \pm 0.01$ RU and $\% \chi^2 = 0.13$. (b) Conventional SPR curves (black) for interaction of soluble target with a hydrogel-bound probe and fit to a two-compartment 1:1 interaction model (red) for estimation of k_a' and k_d' . Target was injected for 60 s in duplicate over a serial-doubling dilution range from 1 μM to 31 nM. All parameters were fit globally returning values of $k_a' = 8.5 \pm 0.004$ ($\times 10^4$) $\text{M}^{-1}\text{s}^{-1}$, $k_d' = 0.075$ s^{-1} , $R_{\text{max}} = 4052 \pm 0.001$ RU and $\% \chi^2 = 0.31$. (c) Estimation of R_{max} from the target-loading phase of rebinding curves. Briefly, 500 nM target was injected over a probe-coated surface ($n = 8$) at 30 $\mu\text{L}/\text{min}$ for 60 s followed by dissociation. A simple 1:1 model was fit returning an estimate of the saturation response, $R_{\text{max}} = 1025 \pm 10$ RU. (d) Inhibition phase region of curves in (c) when dissociation was ≤ 118 RU, the injection point for a rebinding inhibitor. The eight curves correspond to the late dissociation phase of the target-loading curves in (c) for duplicate injections of inhibitor at 0 μM , 0.016 μM , 0.6 μM and 4 μM . Curves (black) were time-normalized at 118RU and fit (red) to equation (4) returning $k_a = 3.07 \pm 0.01$ ($\times 10^6$) $\text{M}^{-1}\text{s}^{-1}$, $k_t = 10.55$ s^{-1} and $\% \chi^2 = 1.1$, where k_a' , k_d' , k_d and R_{max} were held constant at the values estimated from (a), (b) and (c). R_0 was fit locally and both k_a and k_t were fit globally. Note: Limited compound solubility prevented use of higher inhibitor concentrations.

Estimation of transient kinetics. In principle, it is possible to maintain inhibition of rebinding when $k_d > k_t$ through rapid alkylation of the inhibition complex, where $k_{inact} > k_d$ and $k_{inact} > k_t$, leading to a partitioning function $z = (1 + k_{inact}/k_t)$. However, such high k_{inact} values are highly unfavorable in drug discovery due to their non-specific alkylation potential and therefore we consider only $k_{inact} < 1 \text{ s}^{-1}$, allowing z to be neglected. Therefore, estimation of k_a and k_d for transient irreversible binding remains identical to reversible inhibitors. To illustrate this, we added an irreversible inhibition complex (**AB***) to the computational model (see Supplemental Note Virtual Instrument) such that formation of an irreversible inhibition complex (**AB***) proceeds at rate constant k_{inact} , where $d\mathbf{AB}^*/dt = k_{inact}\mathbf{AB}$. Inhibition curves at six k_a values were replicated ($n = 8$), at four transient binding levels ($0.1 \leq k_d \leq 10 \text{ s}^{-1}$) with, and without, inclusion of irreversible alkylation ($k_{inact} = 1 \text{ s}^{-1}$) for a total of forty eight separate conditions. As shown in Fig. 5a, the resulting forty eight inhibition curves superimpose almost perfectly at each k_a value, indicating that the rebinding assay may be expected to return k_a estimates using equation (4) without inclusion of a partition function while $k_t \gg k_d$, or $k_t \gg k_{inact}$ hold.

As shown in Fig. 5b, inhibition of transient inhibitors will decrease when k_t is in the same order, or less than k_d and follows a partition function $f = \frac{1}{1 + k_d/k_t}$, where total hydrogel escape is $\beta = k_t + f.k_a.A$. It also implies that the measurable k_d -range may be increased by employing conditions that promote a wider range in k_t (see equation (2)) and modulating secondary non-specific transient interactions between the hydrogel and the target. The surrogate experimental data in Fig. 5c, d assume a dissociation phase beginning at 10% of saturation $R_0 = 0.1R_{max}$ and exhibit low systematic error (< 5%) over 2-orders for simultaneous estimation of k_a and k_d . Higher R_0/R_{max} results in higher measurement error, as shown in Fig. 5e, f. Multiple dissociation phase curves were generated over a range in R_0/R_{max} , were response-normalized (Fig. 5e) and show a maximum divergence of ~6% occupancy at $R_0/R_{max} = 1$ with negligible divergence for $R_0/R_{max} \leq 0.25$. Propagation of this systematic deviation into error in kinetic parameter return was evaluated by fitting equation (4) to surrogate experimental data over a wide range in R_0/R_{max} , as shown in Fig. 5f. The lowest systematic error was observed for k_a -estimation when k_d was held constant, resulting in a maximum of 13% underestimation at $R_0/R_{max} = 1$, while < 4% error was observed at $R_0/R_{max} < 0.2$. This error is related to divergence of the dissociation curves, when $R_0/R_{max} > 0.2$, causing a ~2-fold increase in systematic deviation when both k_a and k_d were fit simultaneously, though this remains within an acceptable error range (< 1.3-fold error) for drug discovery applications. These results are expected as the magnitude of heterogeneous rebinding regimes¹⁹ exhibiting multiphasic dissociation increases when dissociation traverses a wider occupancy range.

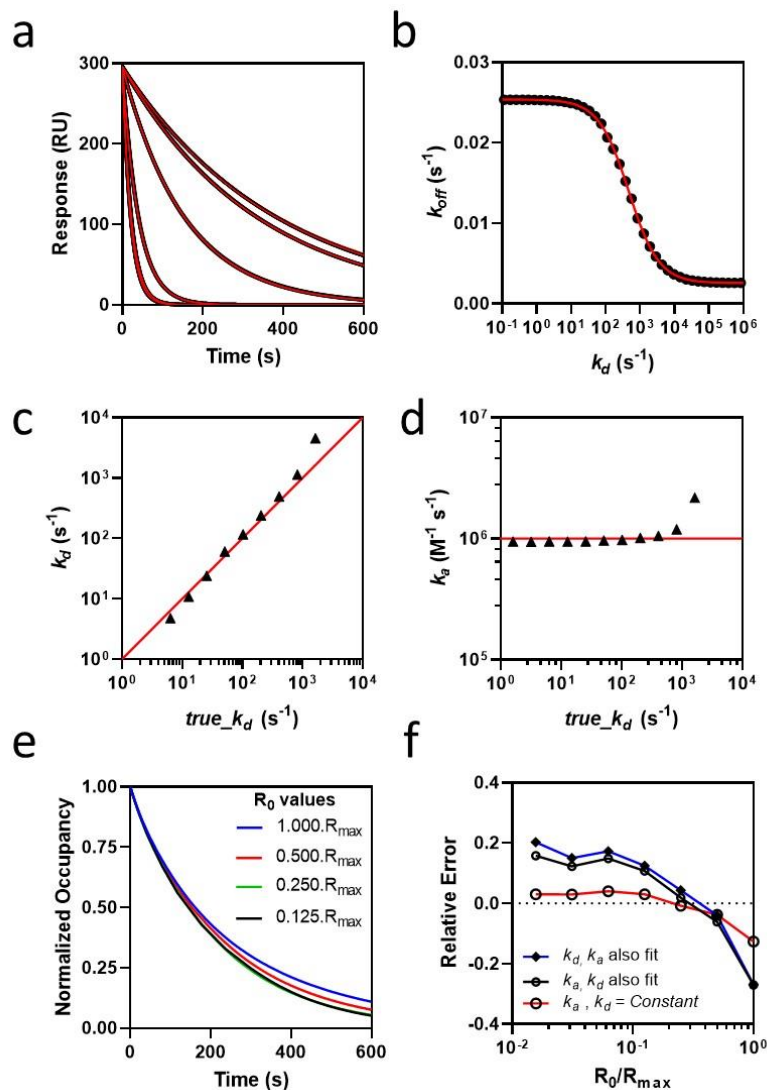


Fig. 5. Kinetic detection limits for transient inhibitor binding. (a) Inhibition curves corresponding to k_a values of 10^4 , 10^5 , 10^6 , 10^7 , 10^8 and 10^9 ($\text{M}^{-1}\text{s}^{-1}$) each with eight superimposable replicates corresponding to k_d (0.0, 0.1, 1.0, 10.0 (s^{-1})) all with, and without, inclusion of an irreversible adduct formation rate $k_{inact} = 0 \text{ s}^{-1}$, or 1 s^{-1} , respectively. The degree of inhibition increased with increasing k_a and inhibition curves superimpose at full inhibition, corresponding to the two highest k_a values of $10^8 \text{ M}^{-1}\text{s}^{-1}$ and $10^9 \text{ M}^{-1}\text{s}^{-1}$, respectively. (b) Partition curve for loss of inhibition of rebinding as a function of transient k_d , where the apparent dissociation rate constant k_{off} was obtained by fitting equation (3) to surrogate experimental data over a range in k_d at $k_a = 1 \times 10^6$ ($\text{M}^{-1} \text{s}^{-1}$). (c) Correlation of k_d returned from fitting equation (4) versus the corresponding true values used in generating the parent surrogate data, where both kinetic constants were constrained as global values for each curve set. Each curve set contained three replicate injections of 1 mM **A**, performed at flow rates 0.1 m/s, 0.01 m/s, 0.001 m/s, respectively. k_t was determined at each flow rate using blank inhibition curves, where **A** = 0, and was then held constant for estimation of kinetics. (d) Correlation of k_d against k_a for the analysis given in (c). (e) Divergence of response-normalized dissociation curves over a range in R_0/R_{max} , where **A** = 0. (f) Relative error in kinetic parameters returned from fitting equation (4) to surrogate experimental data over a wide range in R_0/R_{max} . Plots (c, d & f) include error bars \pm parameter fitting error but are too low to be visible. See Supplemental Note Fig. 5 for more details.

Limit of detection and parameter return for rebinding assay relative to competitive kinetics.

Monte Carlo simulations seeded with pairs of pseudo-random kinetic values were generated to compare the solution phase competitive kinetic binding model of Motulsky-Mahan²⁰ with the rebinding assay given by equation (4). For each assay format, the iso-response contours on the top left-hand corner define the sensitivity limit and indicate a broad measuring range. For competitive kinetics shown in Fig. 6a, the diagonal iso-response contours are affinity isotherms that dominate affinity space while vertical iso-response contours are confined to an affinity region composed of tightly bound inhibitors (bottom right-hand corner), indicating k_a -driven inhibition. Conversely, as shown in Fig. 6b, vertical iso-response contours are observed for the rebinding assay indicating fully k_d -independent k_a -determination over the majority of affinity space. Affinity isotherms are confined to extremely transient affinity space because such transient complexes approach steady-state faster than the inhibitor can escape the hydrogel, subject to partition f .

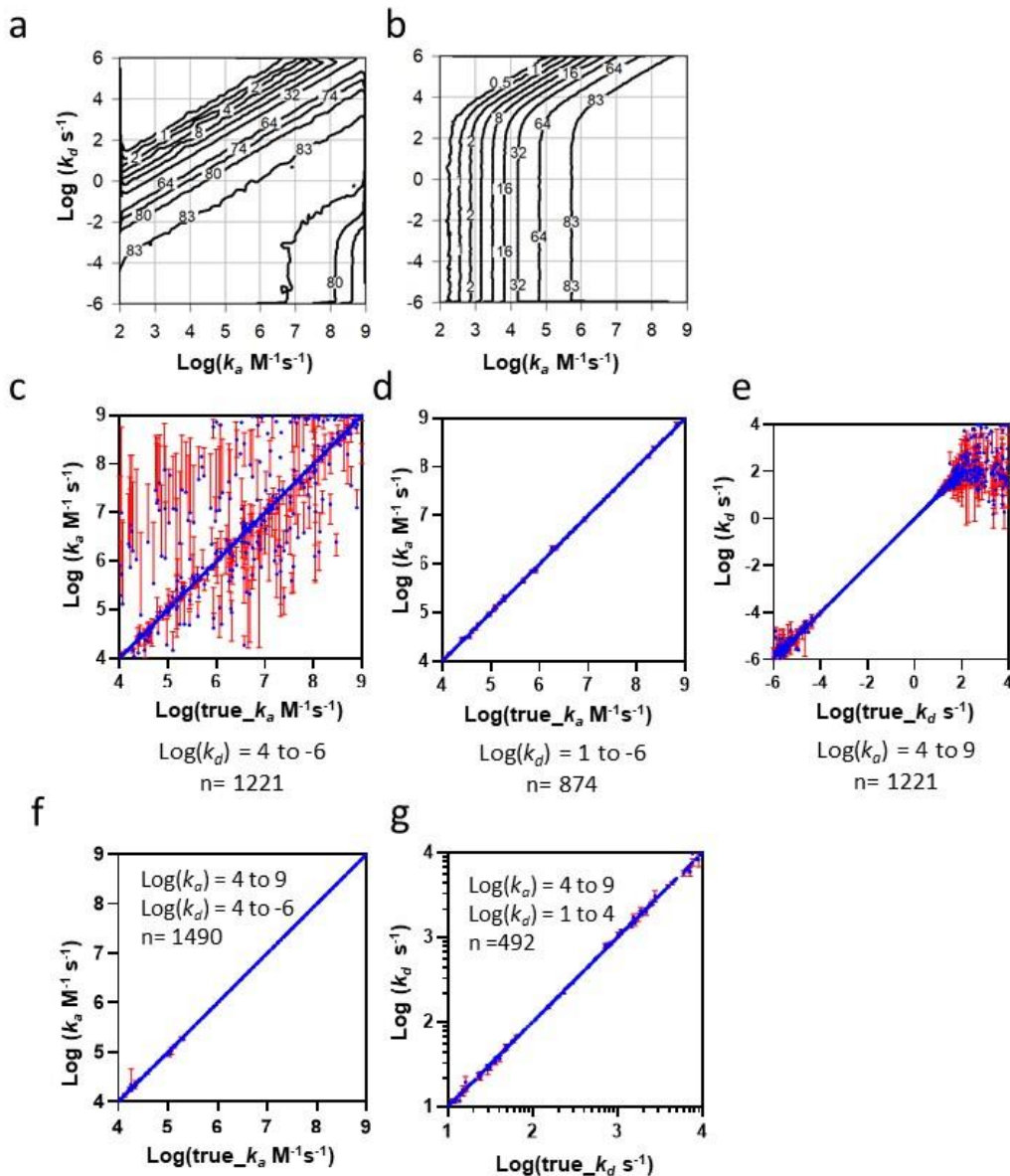


Fig. 6. Comparison of the competitive kinetics assay with the rebinding assay in terms of sensitivity and parameter estimation, evaluated using Monte Carlo simulations seeded with pairs of pseudo-random kinetic values. (a) Affinity space plot for competitive kinetics with contour curves connecting regions of equal response (response value (RU) is inset on contour curves). (b) As in (a) but replicated for the rebinding assay format. (c) Correlation of $true_{k_a}$ versus k_a returned from fitting the competitive kinetic model, associated with the parent Monte Carlo simulation, for pseudo-random k_a/k_d combinations spanning 10-orders with limits $4 \leq \text{Log}(k_a) \leq 9$ and $-6 \leq \text{Log}(k_d) \leq 4$. The diagonal, or unit slope, indicates the accuracy of parameter return and the standard error associated with the parameter fit is indicated by the \pm SE bars. (d) Data set given in (c) where k_a/k_d combinations containing transient k_d values were eliminated by restricting the k_d limit to $-6 \leq \text{Log}(k_d) \leq 1$. (e) As in (d) but given in terms of the fitted k_d versus the true- k_d . (f) Correlation of fitted k_a versus the $true_{k_a}$ for the rebinding assay format. Assay parameters for the Monte Carlo simulations were matched with competitive kinetics in (c) and are shown over the full kinetic range given by limits $4 \leq \text{Log}(k_a) \leq 9$ and $-6 \leq \text{Log}(k_d) \leq 4$. (g) Correlation of fitted k_d versus the $true_{k_d}$ for the rebinding assay in (f), where k_d was restricted to transient k_d values over the limit $1 \leq \text{Log}(k_d) \leq 4$. See Supplemental Note Fig. 6 for more details.

The kinetic measuring range of both formats were evaluated using Monte Carlo simulations²¹ where each respective kinetic model was back-fit to a large set of simulated curve sets produced from each respective parent model and is shown in Fig. 6 c-g. For competitive kinetics, the k_a -correlation plot in Fig. 6c shows that kinetic parameters are poorly defined over a broad range in k_a when k_d is transient, while the remainder of the simulations returned reliable k_a estimates, as shown in Fig. 6d. Furthermore, the k_d -correlation plot in Fig. 6e also shows poor k_d estimates for transient binders. In contrast, the k_a -correlation plot for the rebinding assay shown in Fig. 5f indicates that k_a remains well defined over the full k_a -range and included highly transient binders. In addition, the associated k_d -correlation plot shown in Fig. 6g indicates that reliable k_d estimates are returned for transient binders, consistent with the results obtained for surrogate data generated from the full computational model and fitted to equation (4), as shown in Fig. 5d, f.

Discussion

The measurement of transient inhibitor kinetics in a practical drug discovery setting has not been enabled despite three decades of real-time, label-free technologies. For example, early chemical matter is often transiently bound, with rapid development of a steady-state plateau that is devoid of kinetic information. In general, steady-state dose response curves are prone to artifacts and it is self-evident that mechanistic discrimination of high quality hits based on exceeding a threshold k_a would be valuable in prioritizing compounds. The time required to fully displace the volume of the flow cell ($> 0.1s$) defines the upper kinetic limit of available biosensors and system modifications that overcome this limit are not yet commercially available¹¹. This longstanding unmet need has been addressed here without ultra-fast injection/detection systems by exploiting analyte rebinding within a crowded receptor environment, mixed-phase partitioning in a flow injection configuration and development of an algebraic model (equation (4)) of these interdependent processes.

A practical rebinding model for flow injection-based biosensors does not exist and has been complicated by the many physical parameters that define the overall system. For example, thick hydrogels containing high concentrations of binding sites are critical to the rebinding assay but complicate mass transport by introducing a hydrogel resistance term $T\gamma$ ¹⁷. Equations (1-3) show that rebinding is critically dependent on k_t yet it remains impractical to pre-estimate as it requires precise estimates of hydrogel parameters (e.g. H_{gel} , D_{gel} , K_{part}) which are usually unknown. In conventional biosensing, rebinding is an interference that compromises kinetic analyses and injection of a soluble form of bound ligand during the dissociation phase has, on occasion, been employed in an attempt to recover the true dissociation rate constant from simple 1:1 binding curves. Indeed a semi-analytical numerical model was reported²² for this application but was unsuitable for more general applications. While equation (4) has been developed for kinetic analysis of inhibitor-target interactions, it may also be employed for this recovery application by pre-estimating k_a , k_d and k_t and solving for k_d' .

Equation (4) assumes a phenomenological encounter complex²³ that is partitioned between alternative reaction paths and follows from a recently reported self-rebinding model²⁴ for bulk solution phase interactions. Equation (4) extends beyond self-rebinding by accounting for rebinding within a receptor-crowded hydrogel and with mixed-phase partitioning in a flow injection configuration. In common with the well know two-compartment model¹⁴, k_t accounts for mass transport resistance but in our rebinding configuration target is partitioned between surface rebinding and escape as a function of k_d/k_t , thereby providing extraordinary sensitivity to transient kinetics (e.g. ms-time domain). This obviates the need for ultra-fast opto-electronics and enables k_d -independent estimates of k_a for non-transient complexes. Partitioning is strongly dependent on hydrogel dimensions and relative spacing of interactants. Briefly, the escape rate of **B** and **AB** through the diffusion boundary layer is k_t and the probability that **B..P** reforms **BP** before exiting a hydrogel of height H_{gel} is a function of the mean free distance d traveled by liberated **B** before being rebound¹⁷ and is given by $P_r = 1 - \exp[-(H_{gel} / d)]$, where $d = (D_{gel} \cdot K_{part} / (k_a \cdot P))^{0.5}$. In the case that $d \ll H_{gel}$, as for a thick hydrogel and/or a high reaction flux coefficient ($k_a \cdot P$), then $P_r \cong 1$ and reformation of **BP** is favored. However, when $d \gg H_{gel}$ then $P_r \cong 0$ and escape of **B** from the hydrogel is favored.

A finite element-based biosensor model simulating a realistic flow-injection-based biosensor system (see Supplemental Note Virtual Instrument for more details) was developed to produce surrogate experimental data over extensive parameter ranges. Advection in bulk flow and diffusion/reaction within the extended hydrogel matrix were modeled as coupled domains of defined volume, where species advection and reaction fluxes were computed to generate realistic surrogate experimental data. These data sets allowed development and validation of the algebraic rebinding model since all kinetic rates are known a priori, which is challenging to achieve experimentally. In agreement with equations (1) and (2), surrogate rebinding data showed that k_t increased exponentially with decreasing hydrogel thickness H_{gel} and increased at higher flow velocities with $v_c^{1/3}$ scaling.

The rebinding model returns k_a estimates that are fully independent of steady-state, or k_d , while $k_d \ll k_t$ and this condition was adopted for analysis of the surrogate rebinding assay data in Fig. 3. The two curve sets in Fig. 3a share identical simulation parameters other than k_a' , giving a 10-fold difference in mass transport limitation. The analysis shows that the rebinding assay measured inhibitor kinetics over a wide range (2.5-3.5 orders) at a single test concentration (Fig. 3a, b). The analysis supports operation in a moderate mass transport limited regime since this allowed inhibition to occur at lower inhibitor concentrations (Fig. 3b) thereby avoiding compound solubility artifacts. This elevated parameter return error (Fig. 3b, c) but k_a estimates were nevertheless returned with < 1.2 -fold relative error and with narrow ($< 5\%$) confidence limits (assuming 95% confidence interval). While the primary objective of the current work was to develop, and validate, equation (4) using surrogate data from the computational model, we also demonstrate an experimental proof-of-principle as shown in Fig. 4. Indeed, k_a estimated from equation (4) was in good agreement with estimates from direct binding and was cross-validated within the rebinding assay itself by also introducing the probe as the inhibitor species. Experimentally, this proof-of-principle shows that the rebinding assay format is comparable to direct SPR binding in terms of experimental complexity and data analysis. As already mentioned, when $k_d \ll k_a$, then \mathbf{AB} is relatively stable such that it remains independent of both k_d and any slower coupled kinetic reaction rates. The data in Fig. 5a implies that k_a may be measured for complex interaction mechanisms, such as irreversible inhibition, providing a full mechanistic analysis when combined with routine alkylation rate constant measurements (i.e. k_{inact}/K_D , where $K_D = k_d/k_a$, or k_{inact}/K_I , where $K_I = \text{inhibition affinity constant}$). However, when $k_d = k_t$ affinity partitioning results in 50% loss in inhibition (Fig. 5b) and transient partitioning ultimately defines the limit of detection of the assay. However, such partitioning also allows k_a and transient k_d to be measured over 2-orders (Fig. 5c, d). Furthermore, while the assay performs best when $R_0 < 0.1R_{\text{max}}$, holding $R_0 = R_{\text{max}}$ (Fig. 5e, f) generated ~ 1.3 -fold error, an acceptable tolerance for drug discovery applications.

Solution-phase competitive binding kinetics may be described by the analytic model of Motulsky-Mahan²⁰ and assumes formation of a “hot” inhibition complex containing a tracer compound to indirectly report the evolution of the inhibition complex. This format can be replicated for surface sensitive biosensors¹³ by injecting a mixture containing soluble probe, and inhibitor, over a target-coated surface generating a resolvable binding response, assuming a significant refractive index difference exists for binding of the competing probe relative to inhibitor binding. In solution-phase competitive kinetics, the reactions evolve towards steady-state, whereas the rebinding format maintains a k_a -driven regime over a wide range. To explore these contrasting properties, sensitivity analysis was performed for both formats using Monte Carlo-like simulations seeded with random kinetic parameter values, and the results are shown in Fig. 6a, b. The resulting affinity plots show that the rebinding assay reports k_a independently of affinity since the affinity isotherms, typical of competitive kinetics (Fig. 6a), are absent for rebinding (Fig. 6b), except in the case of transient binders, which are detected at 33-fold higher sensitivity. Furthermore, transition from an affinity-independent regime to an affinity-dependent regime can only occur for solution-phase competitive kinetics when the inhibition complex is extremely stable ($k_d < 1 \times 10^{-4} \text{ s}^{-1}$). For the rebinding assay, the affinity-independent regime dominates and can be further extended by increasing k_t and can be accomplished by limiting self-self-interactions, non-specific hydrogel interactions, and enhancing convective/diffusive transport within the hydrogel-flow cell system. Monte Carlo simulations were also performed to test the limits of kinetic parameters returned by each format. The data showed that solution phase affinity (Fig. 6c, d, e) did not return reliable kinetics for transient binding ($k_d > 10 \text{ s}^{-1}$), whereas the rebinding format accurately returned both k_a and k_d for such transient binders (Fig. 6f, g), while reporting affinity independent k_a for non-transient binding. In summary, a rebinding assay exploiting flow-injection-analysis was developed relying on a flux balance of target partitioned between rebinding and escape within a hydrogel film. The method is well suited to

resolving both k_a and k_d of transiently bound complexes, which remain challenging to measure in a contemporary drug discovery setting, providing mechanistic discrimination of artifactual binding with adequate throughput for practical applications. An experimental proof-of-principle demonstrated estimation of k_a that was independent of both k_d and steady-state thereby establishing the feasibility of measuring extremely rapid association kinetics for non-transient binding complexes.

Methods

Experimental proof-of-principle for estimating k_a of non-transient inhibitors. Assays were conducted using a Biacore S200 (GE Healthcare Bio-Sciences AB, SE-751 84, Uppsala, Sweden) with analysis temperature set to 20 °C. All reagent coupling kits and sensors were from GE Healthcare. A biotinylated-avi-tagged 22 kDa target protein was, expressed recombinantly and purified in-house using standard protocols. The probe molecule ($M_r = 737$ Da) was a PEGylated compound with moderate affinity for the target where a terminal primary amine on the PEG linker allowed coupling to a CM5 sensor chip through standard EDC/NHS covalent linkage chemistry. All experiments were performed using an assay buffer containing 50 mM 4-(2-hydroxyethyl)-1-piperazineethanesulfonic acid, (HEPES), pH 7.5, containing 0.15 M sodium chloride and 0.2 mM tris(2-carboxyethyl)phosphine (TCEP), 0.1% polyethyleneglycol ($M_n \sim 4$ kDa), 1 mg/ml CM dextran ($M_n \sim 10$ kDa).

Kinetics of probe binding to tethered target. Target was captured onto a series S SA sensor chip. The soluble probe was injected for 30 s in duplicate over a serial doubling dilution range from 1 μ M to 31 nM prepared in assay buffer. The binding curves were double referenced and fit to a two-compartment 1:1 interaction model (red) for estimation of k_a and k_d .

Kinetics of target binding to tethered probe. Channels 2 and 4 of a series S CM5 sensor chip were activated in-situ for 8 min using standard EDC/NHS. The chip was undocked, rinsed with buffer and 40 μ l of probe solution containing 1 mM probe, diluted in a 1:1 (v/v) solution of DMSO:1M HEPES (pH 7.5), was pipetted onto the sensing surface and incubated for 2 h at room temperature. The surface was rinsed in buffer and blocked with 1 M ethanolamine for 10 min. The chip surface was rinsed with 100% DMSO, 20 mM NaOH and ultrapure water, dried and redocked. Target protein diluted in assay buffer was injected for 60 s in duplicate over a serial-doubling dilution range from 1 μ M to 31 nM.

Rebinding assay curves. A fresh probe-coated CM5 sensor chip was prepared, using a 20 min probe-solution contact time, which lowered the R_{max} relative to the previous 2 h exposure. 500 nM target was injected over channel 2 (probe-coated) at 30 μ L/min for 60 s followed by dissociation. This was repeated (8 replicates) and the target was allowed dissociate from the surface between replicate cycles. An inhibitor injection commenced for each of these target-loading injections when the dissociation response decreased to 118 RU. The inhibitor was injected over channels 1 and 2, in duplicate, at 0 μ M, 0.016 μ M, 0.6 μ M and 4 μ M with assay buffer as diluent.

All other methods. See Supplemental Notes for more details on all other methods.

References

1. McGovern, S.L., Caselli, E., Grigorieff, N. and Shoichet, B.K.A. Common mechanism underlying promiscuous inhibitors from virtual and high-throughput screening. *J. Med. Chem.* **45**, 1712–1722 (2002). <https://doi.org/10.1021/jm010533y>
2. Sink R, Gobec S, Pečar S, Zega A. False positives in the early stages of drug discovery. *Curr. Med. Chem.* **17**, 4231-55 (2010). <https://doi.org/10.2174/092986710793348545>
3. Torosyan, H. and Shoichet B.K.A. Protein Stability Effects in Aggregate-Based Enzyme Inhibition. *J. Med. Chem.* **62**, 9593-9599 (2019). <https://doi.org/10.1021/acs.jmedchem.9b01019>
4. Copeland R. A. The drug-target residence time model: a 10-year retrospective. *Nat. Rev. Drug Discov.* **15**, 87-95 (2016). <https://doi.org/10.1038/nrd.2015.18>
5. Sykes, D. A. et al. Extrapyramidal side effects of antipsychotics are linked to their association kinetics at dopamine D2 receptors. *Nat. Commun.* **8**, 763 (2017). <https://doi.org/10.1038/s41467-017-00716-z>
6. Amaral, M. et al. Protein conformational flexibility modulates kinetics and thermodynamics of drug binding. *Nat. Commun.* **8**, 2276 (2017). <https://doi.org/10.1038/s41467-017-02258-w>
7. Vauquelin, G. Effects of target binding kinetics on in vivo drug efficacy: koff, kon and rebinding. *Br. J. Pharmacol.* **173**(15), 2319-34 (2016). <https://doi.org/10.1111/bph.13504>
8. Rich, R. L. et al. A global benchmark study using affinity-based biosensors. *Anal. Biochem.* **386**, 194–216 (2009). <https://doi.org/10.1016/j.ab.2008.11.021>
9. Papalia, G. A. et al. Comparative analysis of 10 small molecules binding to carbonic anhydrase II by different investigators using Biacore technology. *Anal. Biochem.* **359**, 94–105 (2006). <https://doi.org/10.1016/j.ab.2006.08.021>
10. Burton, R. L., Hanes, J. W. & Grant, G. A. A stopped flow transient kinetic analysis of substrate binding and catalysis in *Escherichia coli* D-3-phosphoglycerate dehydrogenase. *J. Bio. Chem.* **283**(44), 29706–29714 (2008). <https://doi.org/10.1074/jbc.M805180200>
11. Quinn, J.G. *, Steffek, M., Bruning, J.M., Frommlet, A. & Mulvihill, M. Unlocking latent kinetic information from label-free binding, *Sci. Rep.* **9**, 18389 (2019). <https://doi.org/10.1038/s41598-019-54485-4>
12. Georgi, V., Dubrovskiy, A., Steigele, S. & Fernández-Montalván, A.E. Considerations for improved performance of competition association assays analysed with the Motulsky–Mahan's “kinetics of competitive binding” model. *Br. J. Pharmacol.* **176**, 4731–4744 (2019). <https://doi.org/10.1111/bph.14841>
13. Karlsson, R. Real-Time Competitive Kinetic Analysis of Interactions between Low-Molecular-Weight Ligands in Solution and Surface-Immobilized Receptors, *Anal. Biochem.* **221**(1), 142-151(1994). <https://doi.org/10.1006/abio.1994.1390>
14. Myszka, D.G., He, X., Dembo, M., Morton, T.A. & Goldstein, B. Extending the range of rate constants available for BIACORE: interpreting mass transport influenced binding data. *Biophys. J.* **75**, 583–594 (1998). [https://doi.org/10.1016/S0006-3495\(98\)77549-6](https://doi.org/10.1016/S0006-3495(98)77549-6)
15. Hansen, R., Bruus, H., Callisen, T. H. & Hassager, O. Transient convection, and adsorption in surface-based biosensors. *Langmuir* **28**, 7557–7563 (2012). <https://doi.org/10.1021/la3000763>
16. Goldstein B, & Dembo M. Approximating the effects of diffusion on reversible reactions at the cell surface: ligand-receptor kinetics. *Biophys J.* **68**(4), 1222-30 (1995). [https://doi.org/10.1016/S0006-3495\(95\)80298-5](https://doi.org/10.1016/S0006-3495(95)80298-5)

17. Wofsy, C and Goldstein, B. Effective Rate Models for Receptors Distributed in a Layer above a Surface: Application to Cells and Biacore. *Biophys. J.* **82**, 1743–1755 (2002). [https://doi.org/10.1016/S0006-3495\(02\)75526-4](https://doi.org/10.1016/S0006-3495(02)75526-4)
18. Pol, E. et al. Evaluation of calibration free concentration analysis provided by Biacore™ systems. *Anal. Biochem.* **510**, 88–97 (2016). <https://doi.org/10.1016/j.ab.2016.07.009>
19. Goldstein, B., Coombs, D., He, X., Pineda, A.R., Wofsy, C. The influence of transport on the kinetics of binding to surface receptors: application to cells and Biacore. *J. Mol. Recognit.* **12**, 293–299 (1999). [https://doi.org/10.1002/\(SICI\)1099-1352\(199909/10\)12:5<293::AID-JMR472>3.0.CO;2-M](https://doi.org/10.1002/(SICI)1099-1352(199909/10)12:5<293::AID-JMR472>3.0.CO;2-M)
20. Motulsky, H. J., & Mahan, L. The kinetics of competitive radioligand binding predicted by the law of mass action. *Molecular Pharmacology*, **25**, 1–9 (1984).
21. Metropolis, N., & Ulam, S. The Monte Carlo method. *J. Am. Stat. Assoc.* **44**, 335–341 (1949). <https://doi.org/10.1080/01621459.1949.10483310>
22. He, X., Coombs, D., Myszka, D.G. et al. A Theoretical and Experimental Study of Competition Between Solution and Surface Receptors for Ligand in a Biacore Flow Cell. *Bull. Math. Biol.* **68**, 1125–1150 (2006). <https://doi.org/10.1007/s11538-006-9093-9>.
23. Shoup, D. & Szabo, A. Role of diffusion in ligand binding to macromolecules and cell-bound receptors. *Biophys. J.* **40**, 33–39, (1982). [https://doi.org/10.1016/S0006-3495\(82\)84455-X](https://doi.org/10.1016/S0006-3495(82)84455-X).
24. Paramanathan, T., Reeves, D., Friedman, L. et al. A general mechanism for competitor-induced dissociation of molecular complexes. *Nat. Commun.* **5**, 5207 (2014). <https://doi.org/10.1038/ncomms6207>

Figures

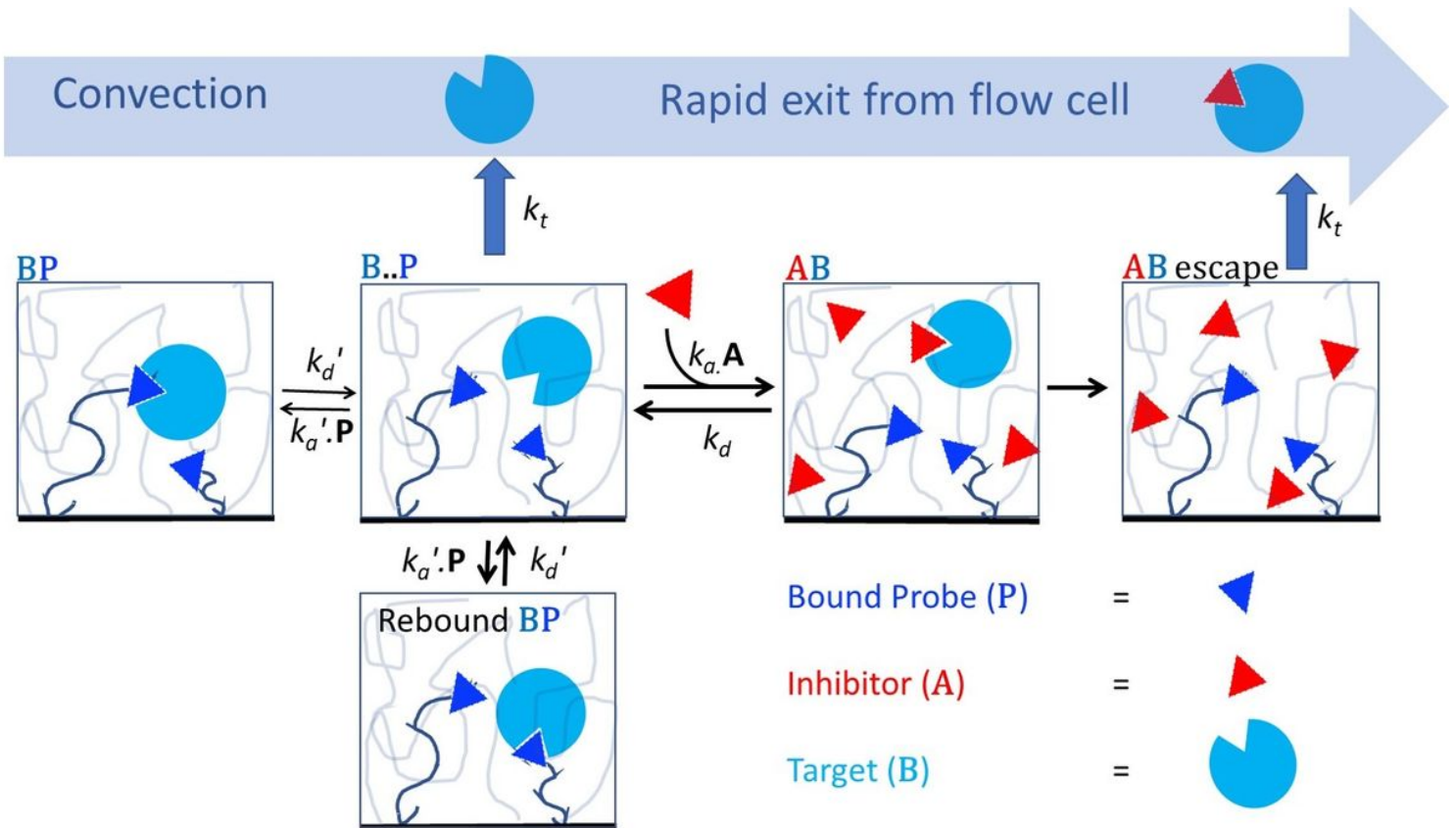


Figure 1

Reaction/diffusion pathways of biosensor-based rebinding-assay. A hydrogel, depicted here as random loops, is derivatized to possess a high concentration of P (blue triangle), which is competitive with inhibitor A (red triangle) in binding to target B (blue circle). Paired forward- and reverse-rate constants for formation of BP and AB are k_a' (M⁻¹s⁻¹)/ k_d' (s⁻¹) and k_a (M⁻¹s⁻¹)/ k_d (s⁻¹), respectively, while k_t (s⁻¹) is the mass transport coefficient that defines the hydrogel escape rate. The molecular contacts stabilizing BP dissociate releasing B to become a transient species B..P that can readily reform BP, pairing with any P in its vicinity. Multiple rebinding cycles are favored at higher concentrations of B and high k_a' before B escapes the sensing region at rate k_t . Injected A sequesters B thereby depleting B..P forming AB, which in turn exits the hydrogel thereby negating rebinding. However, in the case that AB dissociates before exiting, then liberated B will revert to B..P. Although not depicted here, B that has escaped the hydrogel has a probability of re-entering the hydrogel further downstream again replenishing B..P. See Supplemental Note Fig. 1 for more details.

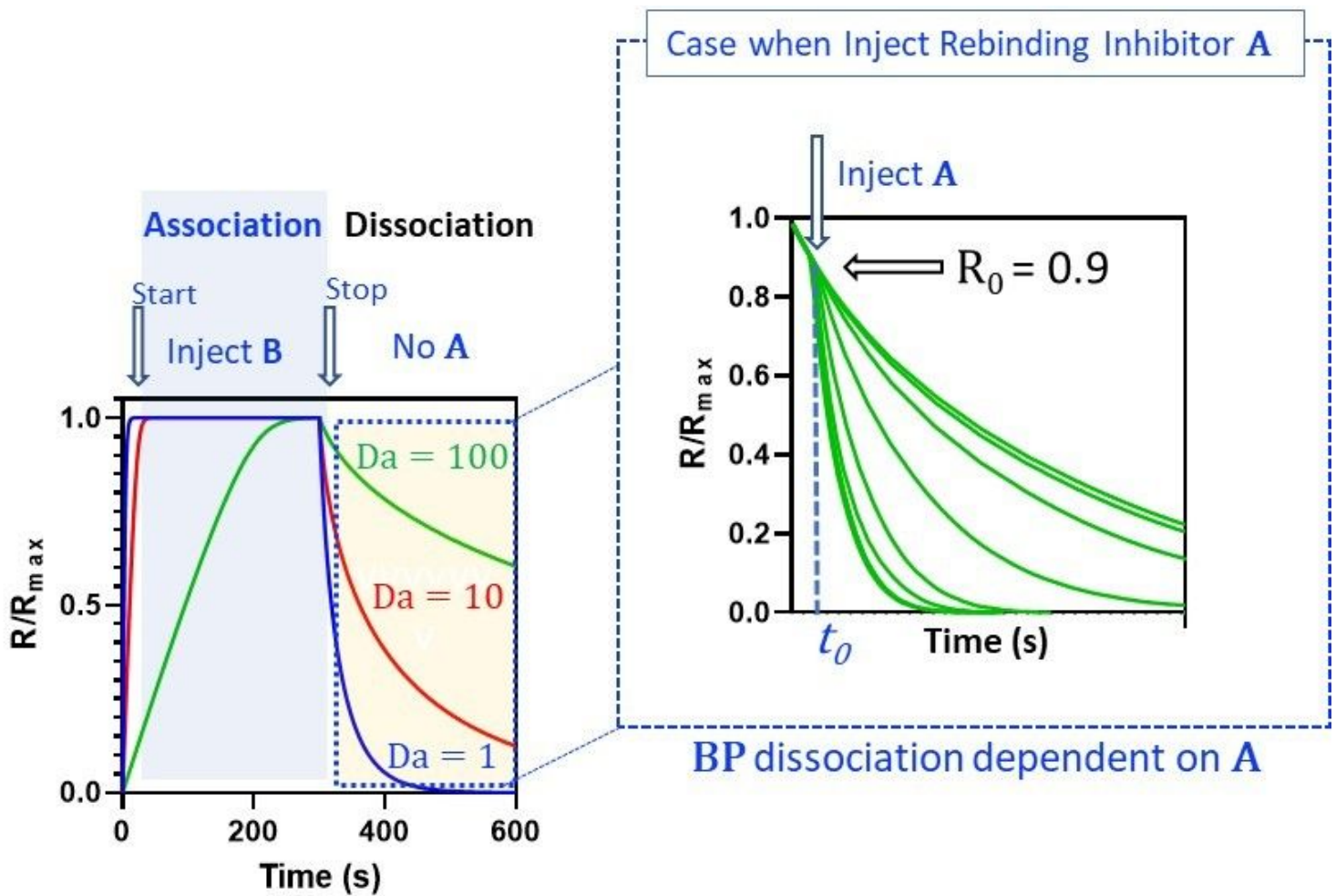


Figure 2

Simulated binding response curves for rebinding and inhibition of rebinding. Three mass transport limited binding curves for 10 nM B binding to P tethered within a hydrogel are shown on the left. The response curves were normalized to the maximum saturation response R_{max} observed before the dissociation phase. The three simulated curves correspond to kt values of $1 \times 10^7 \text{ s}^{-1}$, $1 \times 10^8 \text{ s}^{-1}$ and $1 \times 10^9 \text{ s}^{-1}$, producing Da values of 100, 10, 1, respectively. The simulation was performed using a two-compartment model (see Supplemental Note Fig. 2) and the interaction parameters were $R_{max} = 20 \text{ RU}$, $k_a' = 5 \times 10^7 \text{ M}^{-1}\text{s}^{-1}$ and $k_d' = 0.05 \text{ s}^{-1}$. Inhibition of rebinding during the dissociation phase at a fixed operating condition is depicted on the right, where injection of A over a concentration series causes dose-dependent inhibition of rebinding. The response observed at the onset (t_0) of the inhibitor injection is R_0 . Inhibition curves were simulated using the finite element computational biosensor model and is described in detail in Supplemental Note Virtual Instrument.

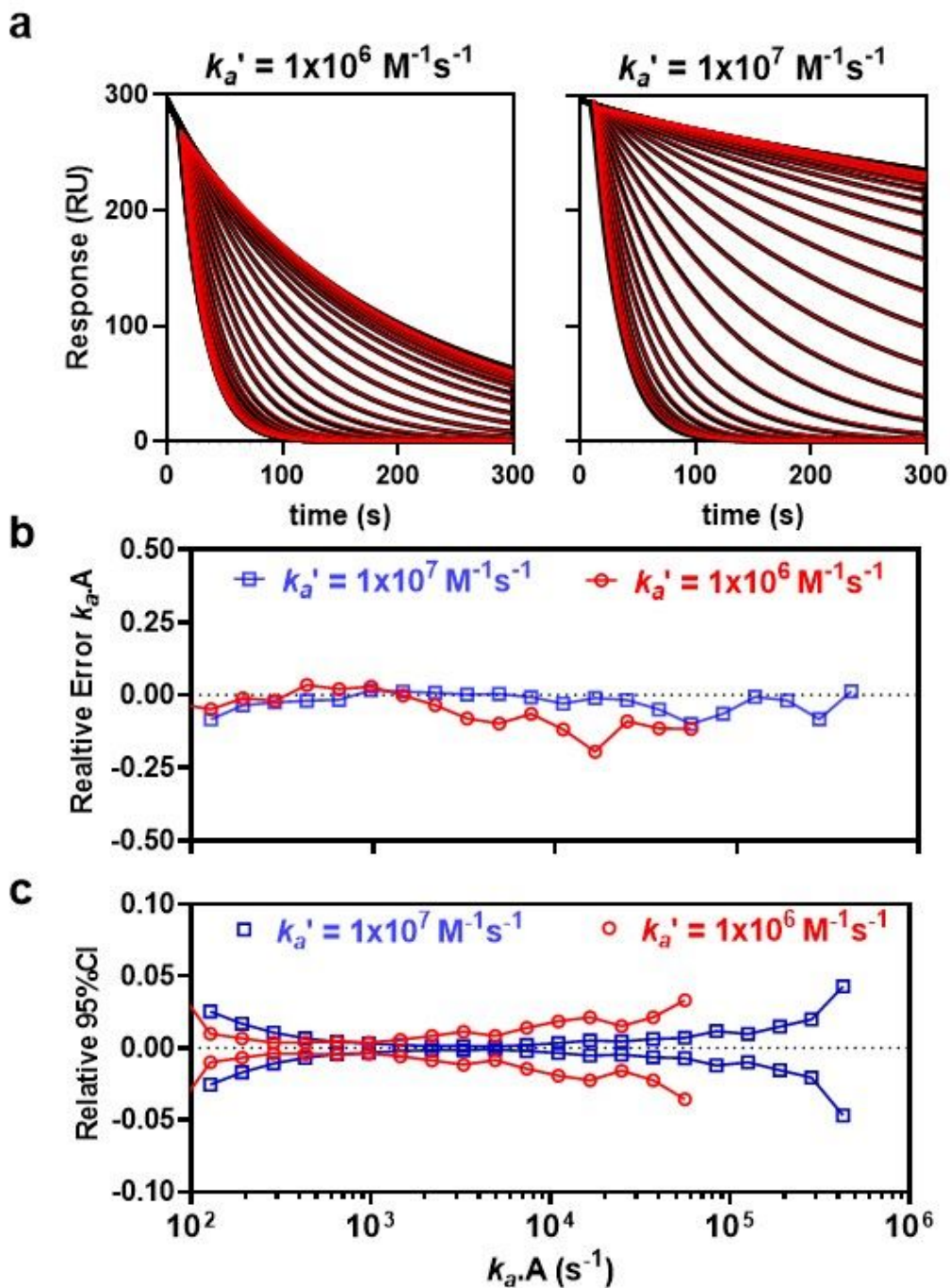


Figure 3

Estimation of k_a from individual inhibition curves at two values of k_a' . (a) Fitted inhibition curves for moderate- (left panel $Da = 8.7$) and high- (right panel, $Da = 87$) mass transport limitation. Inhibition curves (black) were fit (red) to equation (4), where k_a was fit locally, giving independent estimates of k_a for each curve, while all other parameters were held constant. (b) Relative error in $k_a.A$ as a function of true $k_a.A$. All values where absolute relative error was < 0.2 are shown. (c) 95% confidence intervals expressed as a fraction of estimated $k_a.A$ and plotted versus true $k_a.A$ and were < 0.05 . See Supplemental Note Fig. 3 for more details.

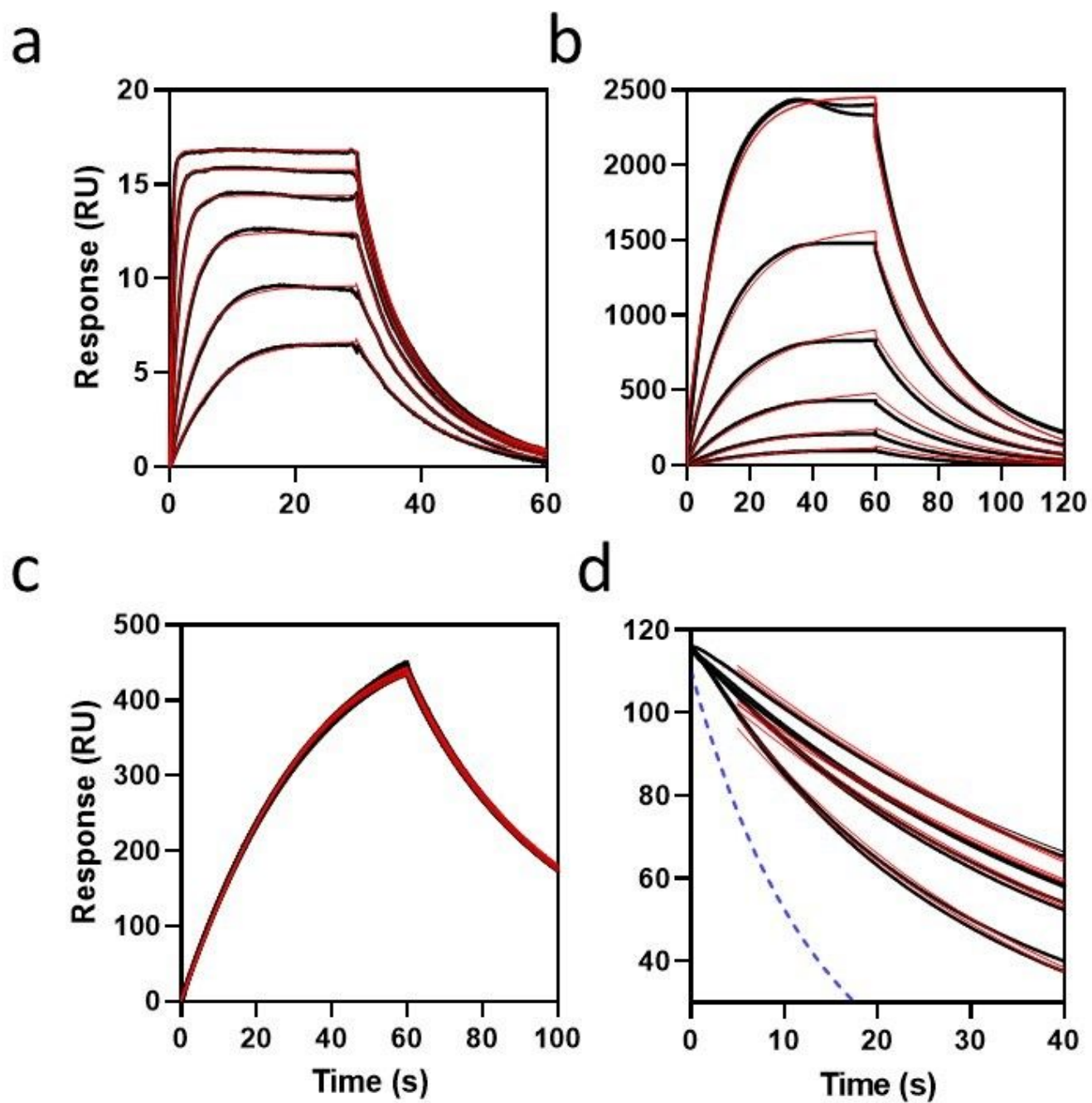


Figure 4

Experimental estimation of k_a using the rebinding assay. Please see manuscript .pdf for full caption.

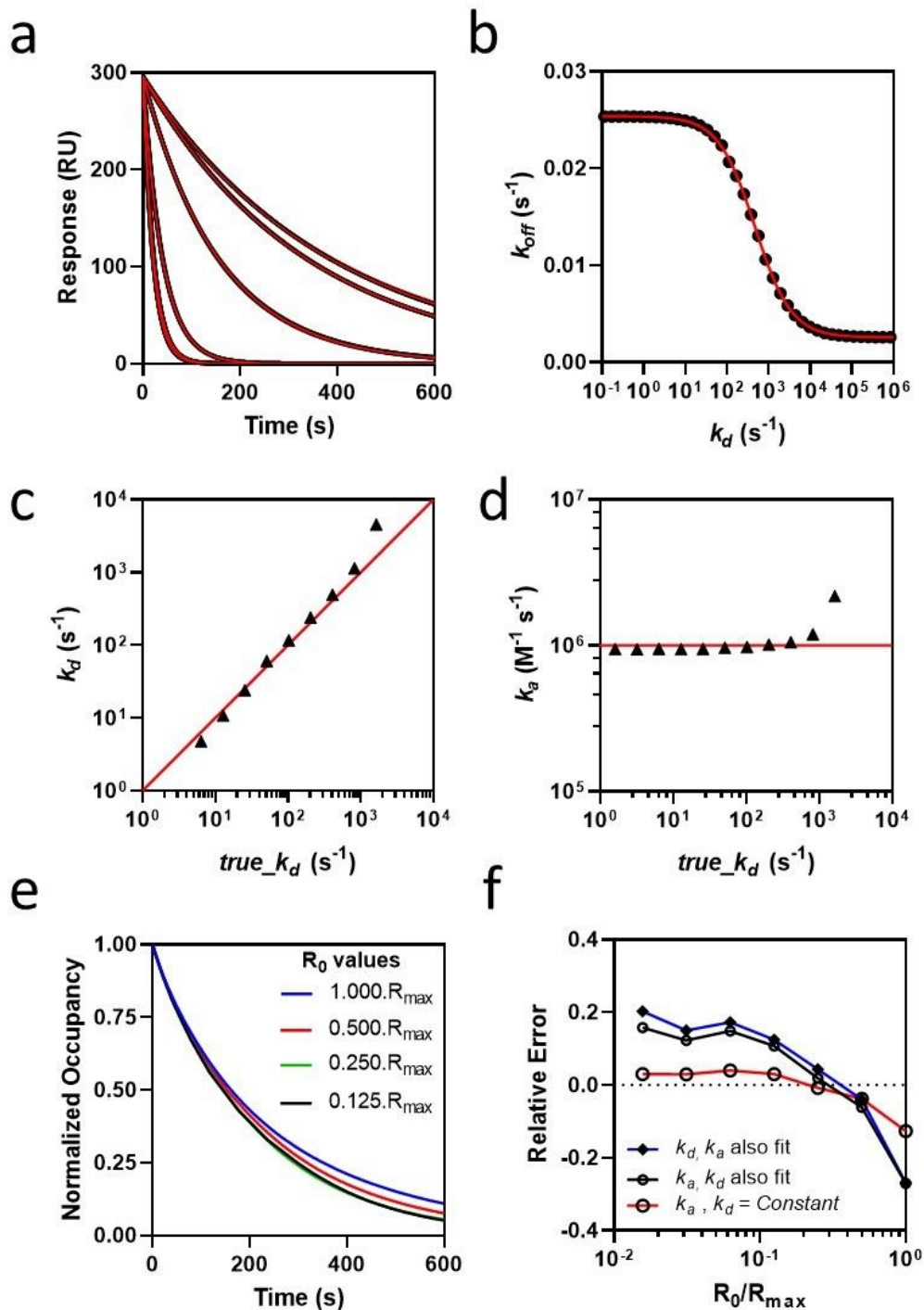


Figure 5

Kinetic detection limits for transient inhibitor binding. (a) Inhibition curves corresponding to k_a values of 104, 105, 106, 107, 108 and 109 ($M^{-1}s^{-1}$) each with eight superimposable replicates corresponding to k_d (0.0, 0.1, 1.0, 10.0 (s^{-1})) all with, and without, inclusion of an irreversible adduct formation rate $k_{inact} = 0 s^{-1}$, or 1 s^{-1} , respectively. The degree of inhibition increased with increasing k_a and inhibition curves superimpose at full inhibition, corresponding to the two highest k_a values of 108 $M^{-1}s^{-1}$ and 109 $M^{-1}s^{-1}$, respectively. (b) Partition curve for loss of inhibition of rebinding as a function of transient k_d , where the apparent dissociation rate constant k_{off} was obtained by fitting equation (3) to surrogate experimental data over a range in k_d at $k_a = 1 \times$

106 (M⁻¹ s⁻¹). (c) Correlation of k_d returned from fitting equation (4) versus the corresponding true values used in generating the parent surrogate data, where both kinetic constants were constrained as global values for each curve set. Each curve set contained three replicate injections of 1 mM A, performed at flow rates 0.1 m/s, 0.01 m/s, 0.001 m/s, respectively. k_t was determined at each flow rate using blank inhibition curves, where $A = 0$, and was then held constant for estimation of kinetics. (d) Correlation of k_d against k_a for the analysis given in (c). (e) Divergence of response-normalized dissociation curves over a range in R_0/R_{max} , where $A = 0$. (f) Relative error in kinetic parameters returned from fitting equation (4) to surrogate experimental data over a wide range in R_0/R_{max} . Plots (c, d & f) include error bars \pm parameter fitting error but are too low to be visible. See Supplemental Note Fig. 5 for more details.

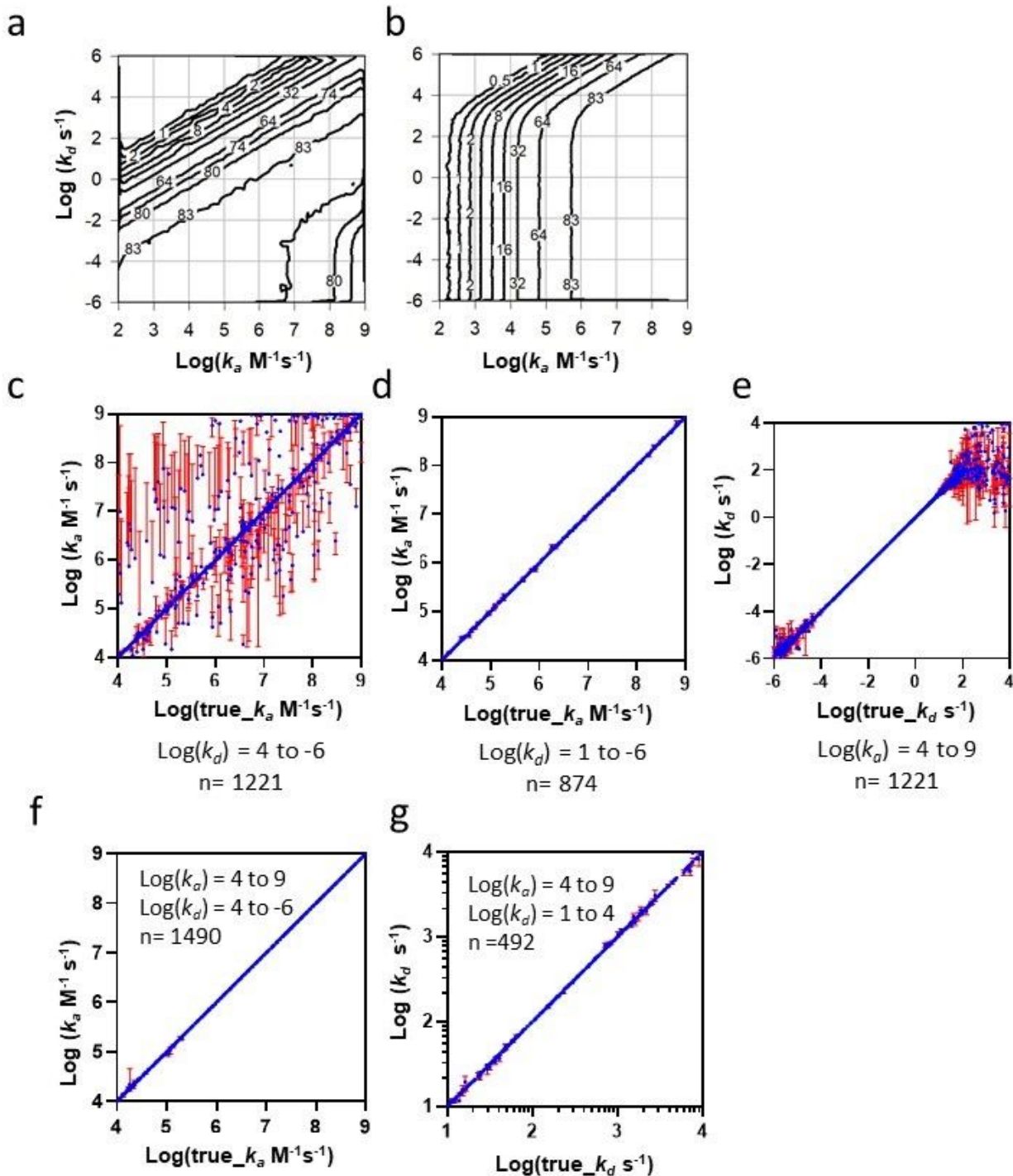


Figure 6

Comparison of the competitive kinetics assay with the rebinding assay in terms of sensitivity and parameter estimation, evaluated using Monte Carlo simulations seeded with pairs of pseudo-random kinetic values. (a) Affinity space plot for competitive kinetics with contour curves connecting regions of equal response (response value (RU) is inset on contour curves). (b) As in (a) but replicated for the rebinding assay format. (c) Correlation of true_ka versus ka returned from fitting the competitive kinetic model, associated with the parent Monte Carlo simulation, for pseudo-random ka/kd combinations spanning 10-orders with limits $4 \leq \text{Log}(ka) \leq 9$ and $-6 \leq \text{Log}(kd) \leq 4$. The diagonal, or unit slope, indicates the accuracy of parameter return and the standard error associated with the parameter fit is indicated by the \pm SE bars. (d) Data set given in (c) were ka/kd combinations containing transient kd values were eliminated by restricting the kd limit to $-6 \leq \text{Log}(kd) \leq 1$. (e) As in (d) but given in terms of the fitted kd versus the true-kd. (f) Correlation of fitted ka versus the true_ka for the rebinding assay format. Assay parameters for the Monte Carlo simulations were matched with competitive kinetics in (c) and are shown over the full kinetic range given by limits $4 \leq \text{Log}(ka) \leq 9$ and $-6 \leq \text{Log}(kd) \leq 4$. (g) Correlation of fitted kd versus the true_kd for the rebinding assay in (f), where kd was restricted to transient kd values over the limit $1 \leq \text{Log}(kd) \leq 4$. See Supplemental Note Fig. 6 for more details.

Supplementary Files

This is a list of supplementary files associated with this preprint. Click to download.

- [SUPPLEMENTALINFORMATIONArebindingassayformeasuringextremekineticsusinglabelfreebiosensors.pdf](#)